Chapter 5
Tides on Satellites of Giant Planets

Nicolas Rambaux and Julie Castillo-Rogez

Abstract The discovery of the satellites of the giant planets started in 1610 when Galileo Galilei pointed his telescope toward Jupiter. Since then observations from Earth- and space-based telescopes and outstanding in-situ observations by several space missions have revealed worlds of great richness and extreme diversity. One major source of energy driving the evolution of these satellites is the gravitational pull exerted by their planets. This force shapes and deforms the satellites and the resulting dissipation of mechanical energy can heat their interiors and drive spectacular activity, such as volcanic eruptions, as for Io or Enceladus. In addition, tides drive orbital evolution by circularizing the satellites' orbits and synchronizing their rotational motions.

5.1 Introduction

The giant planets of the solar system, Jupiter, Saturn, Uranus, and Neptune, have many satellites. So far, astronomers have identified 168 giant-planet satellites[1]: 66 of Jupiter, 62 of Saturn, 27 of Uranus, and 13 of Neptune. All these satellites display a large variety of dynamical configurations and geophysical properties that have been studied by continual ground-based telescopic observations and dedicated space missions *Voyager*, *Pioneer*, *Galileo*, and *Cassini-Huygens* sent by NASA and ESA, with international participation. *Pioneer* and *Voyager* achieved in the 70s and 80s a formidable trip across the outer solar system. They sent the first images of the satellites surfaces, revealing an extraordinary geological richness. Then, *Galileo*

[1] See the regularly update of satellite's number at IMCCE web service http://www.imcce.fr/hosted_sites/saimirror/Nomenclaf.html.

N. Rambaux (✉)
IMCCE, Observatoire de Paris, CNRS UMR 8028, Université Pierre et Marie Curie, UPMC - Paris 06, 77 avenue Denfert-Rochereau, 75014 Paris, France
e-mail: Nicolas.Rambaux@imcce.fr

J. Castillo-Rogez
Jet Propulsion Laboratory, Caltech, Pasadena, CA 91109, USA
e-mail: julie.c.castillo@jpl.nasa.gov

J. Souchay et al. (eds.), *Tides in Astronomy and Astrophysics*,
Lecture Notes in Physics 861, DOI 10.1007/978-3-642-32961-6_5,

Table 5.1 Parameters characterizing outer planet satellites; a denotes the semi-major axis, e the eccentricity, P_{orb} the orbital period and P_{rot} the rotational period, GM the gravity mass, R the radius, and H the equilibrium tide of the satellites. Source: JPL (Jet Propulsion Laboratory) Solar System Dynamics website http://ssd.jpl.nasa.gov. The period of rotation is indicated with a "C" when the rotation is chaotic [120]. The rotational period of Nereid is not accurately determined but certainly in the range 0.8–3 days [96]

Body	a (km)	e	P_{orb} (days)	P_{rot} (days)	GM ($km^3\,s^{-2}$)	R (km)	H (m)
Io	421800	0.0041	1.769	1.769	5959.916	1821.6	3118.8
Europa	671100	0.0094	3.551	3.551	3202.739	1560.8	776.7
Ganymede	1070400	0.0013	7.155	7.155	9887.834	2631.2	500.7
Callisto	1882700	0.0074	16.69	16.69	7179.289	2410.3	89.2
Mimas	185539	0.0196	0.942	0.942	2.5026	198.20	3662.0
Enceladus	238037	0.0047	1.370	1.370	7.2027	252.10	1577.1
Tethys	294672	0.0001	1.888	1.888	41.2067	533.00	2903.5
Dione	377415	0.0022	2.737	2.737	73.1146	561.70	960.6
Rhea	527068	0.0010	4.518	4.518	153.9426	764.30	574.2
Titan	1221865	0.0288	15.95	15.95	8978.1382	2575.50	102.0
Hyperion	1500934	0.0232	21.28	C	0.3727	135.00	10.0
Iapetus	3560851	0.0293	79.33	79.33	120.5038	735.60	2.0
Phoebe	12947913	0.1634	550.30	0.45	0.5532	106.60	0.004
Miranda	129900	0.0013	1.413	1.413	4.4	235.8	1857.3
Ariel	190900	0.0012	2.520	2.520	86.4	578.9	1082.6
Umbriel	266000	0.0039	4.144	4.144	81.5	584.7	441.5
Titania	436300	0.0011	8.706	8.706	228.2	788.9	118.4
Oberon	583500	0.0014	13.46	13.46	192.4	761.4	50.9
Triton	354759	0.0000	5.877	5.877	1427.6	353.4	1.7
Nereid	5513818	0.7507	360.13	< 3	2.06	170	0.02

(1993–2003) and *Cassini* (2004-today) were dedicated to the Jupiter and Saturnian systems, respectively, performing extensive observations and permitting a greater understanding of the relationships between planets, rings, and satellites. Here, we focus on large regular satellites with radii larger than 100 kilometers. The satellites' main physical and dynamical properties are gathered in Table 5.1. Figure 5.1 represents the satellites as a function of their relative sizes, densities, and distance to the parent-planet expressed in planetary radius. The sizes of the satellites range from 2631.2 km for Ganymede (larger than Mercury) to 106.6 km for Phoebe. Satellite densities reflect their internal composition ranging from 3.6 $g\,cm^{-3}$ for Io, dominated by silicates and a large metallic core, to 0.97 $g\,cm^{-3}$ for water-dominated Tethys. Intermediate densities reflect variations in the relative fractions of ice, silicates, and porosity. The rock mass fraction determines in part the amount of tidal

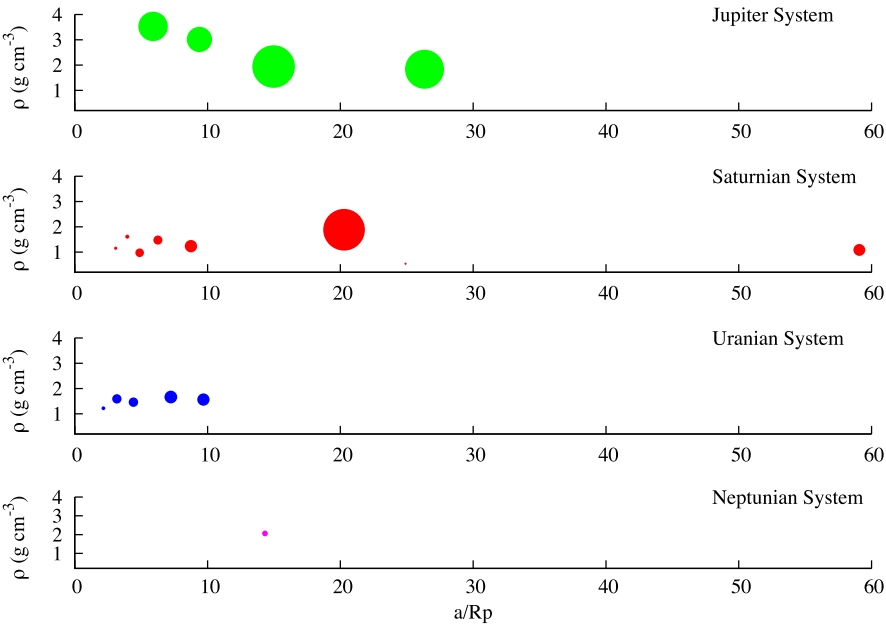

Fig. 5.1 Satellite density as a function of the distance to the parent-planet (expressed in planetary radius). The relative size of the satellites is respected but is not to scale with the distance. From *left* to *right* and *top* to *bottom*: Io, Europa, Ganymede, Callisto; Mimas, Enceladus, Tethys, Dione, Rhea, Titan, Hyperion, Iapetus; Miranda, Ariel, Umbriel, Titania, Oberon; Triton. The satellites Phoebe and Nereid are not represented because they are far from their planets (215 Saturn's radii and 223 Neptune's radii, respectively)

dissipation expected in these objects, as ice is generally more dissipative than silicates.

From Table 5.1 and Fig. 5.1, we can see that most satellites are close to their parent-planets and thus may experience significant tidal stressing. The tidal force results from the amplitude of the gradient of the external gravitational field between the sub-planet and the anti-planet hemispheres. This tidal force distorts the satellite, if it is not rigid, so that the amplitude of the *equilibrium tide* is expressed through [79]

$$H = R_s \frac{M_p}{M_s} \left(\frac{R_s}{d} \right)^3 \tag{5.1}$$

where R_s and M_s are the radius and mass of the satellite, M_p is the mass of the planet, and d is the distance between the satellite and its parent-planet. Here, the amplitude is expressed for a particle where the tide-generating body is at the zenith. The *equilibrium tide* represents the ratio between the external gravitational potential and the gravity of the body. The displacement at the surface is obtained by multiplying H by the secular Love number that represents the ability of the body to deform when in hydrostatic equilibrium (see Sects. 5.4 and 5.5). In the case of a

homogeneous body this factor, labeled h_2, is equal to $5/2$. It decreases with increasing concentration of the density toward the center of the object. The tidal bulge H increases with the size of the object and decreases with the distance to the primary. The equilibrium tide is 3.6 km for Mimas, then around 3 km for Io and Tethys, and then decreases to a few meters for those small satellites located beyond 10 planetary radii, as shown in Table 5.1.

The planet is also subject to an equilibrium tide exerted by its satellites. The combined planet and satellite tides drive the evolution of the satellite's orbit, making it contract or expand depending on the dissipation within each body. For most satellites, the tides lead to orbit circularization. If the satellite is close to its parent-planet, then the orbit evolves toward the planet's equatorial plane, whereas for distant satellites subject to little dissipation the equilibrium plane is intermediate between the planet's equatorial and orbital planes [87]. In addition, the tides raised on the satellites lead to despinning. Most large satellites (apart from Phoebe and Nereid) are in synchronous spin-orbit resonance, i.e. the orbital and rotational periods are equal on average. As a consequence, the satellites show on average the same face toward the planet, like the Moon toward the Earth.

For a satellite in spin-orbit synchronous resonance, the secular part of the tidal potential elongates the body along the planet-satellite axis. In cooperation with the centrifugal potential this flattens the poles of the satellite; the resulting equilibrium figure is then a triaxial ellipsoid. Under the assumption of hydrostaticity, the equilibrium figure brings information on the density structure of the body. Departure from hydrostaticity may inform on the geophysical and dynamical evolution of the object (e.g. fossil shape, mass anomalies, etc.).

The periodic part of the tidal potential deforms the body continuously and leads to solid friction within the material. The amount of friction is a function of the orbital eccentricity. The consequences of that process can be spectacular, such as volcanic activity as observed on Enceladus or Io. Other outstanding signatures of tides can be found on the surface of Europa, related to faults and cycloid cracks. The heating resulting from tidal friction is also believed to play a role in the origin and/or preservation of subsurface oceans in Europa, Ganymede, Titan, Triton ([49] and references therein). Callisto is far from Jupiter so the tidal dissipation in that object is small. However, the presence of an internal ocean has been suggested based on *Galileo*'s magnetometer data. Its long-term preservation is explained by slow heat loss [69]. Oceans inside Rhea, Titania, Oberon have been suggested but this is still debated, in absence of observational constraints [49]. These geological and geophysical consequences are described in many very good reviews on satellites (e.g. [16, 49, 87, 105]; and the book on icy satellites by Grasset et al. [38]).

This chapter is divided in four sections following this introductory Sect. 5.1. In Sect. 5.2, we outline a simple version of the tidal theory that is a toy model useful for conveying the main concepts and illustrating the consequences of tidal friction. Section 5.3 describes the influence of the tides on the dynamical evolution of satellites. The equilibrium figure of a satellite resulting from tidal distortion is described in Sect. 5.4, and in Sect. 5.5 we describe and discuss the consequences of tidal dissipation in icy satellites.

5.2 Tidal Potential

The historical developments leading to the modern formulation of tidal modeling can be found in Chap. 2 of the present volume. The modern treatment of the solid body tides began with a seminal series of papers written by Darwin [19, 20]. Since this pioneering work, tidal modeling has been extensively explored in the literature (e.g. [35, 37, 51, 55, 65, 72–74]). Recent laboratory measurements of the response of planetary materials to cyclic forcing (e.g. [67] for a review) has lead to reviewing the tidal theory (e.g. [28, 29, 31]). Traditionally, the tidal theory is developed from the tide-generated disturbing potential into Fourier series, and a dissipative component is related to each term. Here, for the sake of simplicity, we follow the approach of MacDonald [65], in which dissipation is modeled in the form of a constant phase lag. However one has to keep in mind that this approach implicitly assumes a certain rheology for the material (response to stress) that can lead to unphysical situations (see the review in [31] and [29]).

Now, we outline the main aspects of the tidal theory used in this chapter. The giant planets and their natural satellites are not point-mass bodies, as generally assumed in ideal mechanical systems, and they deform under the gravitational acceleration of external bodies. For a satellite S of radius R_s, the mean gravitational acceleration due to the planet P is the vector $GM_p\mathbf{SP}/SP^3$ where G is the gravitational constant and M_p the mass of the perturbing body, i.e. the parent-planet in the present case. For each element of the satellite M the relative distance between the element and the planet is the vector $\mathbf{MP}$. Consequently the net tidal acceleration $\mathbf{g}^T$ experienced by the element is

$$\mathbf{g}^T = GM_p\left(\frac{\mathbf{MP}}{MP^3} - \frac{\mathbf{SP}}{SP^3}\right). \tag{5.2}$$

It is a differential acceleration. By setting $\mathbf{SP} = \mathbf{d}$ and $\mathbf{SM} = \mathbf{x}$ the vector position of an element in the satellite, $\mathbf{MP}$ may be decomposed as $\mathbf{MP} = \mathbf{SP} - \mathbf{SM} = \mathbf{d} - \mathbf{x}$, leading to the approximation for small values of $|\mathbf{x}|$

$$MP^{-3} \approx d^{-3}\left(1 + 3\frac{\mathbf{d}}{d}.\frac{\mathbf{x}}{d}\right). \tag{5.3}$$

Injecting this expression into Eq. (5.2), we obtain

$$\mathbf{g}^T = \frac{GM_p}{d^3}\big(3(\mathbf{x}.\mathbf{e})\mathbf{e} - \mathbf{x}\big), \tag{5.4}$$

where $\mathbf{e} = \mathbf{d}/d$ is the unit cosine vector. The Cartesian expression of the tidal force in the rotating reference frame of the satellite is then

$$\mathbf{g}^T = \frac{GM_p}{d^3}(2x_p, -y_p, -z_p). \tag{5.5}$$

The gravitational force is then stronger on the x_p direction that points toward the perturbing body and negative in the y_p and z_p directions. This tidal acceleration

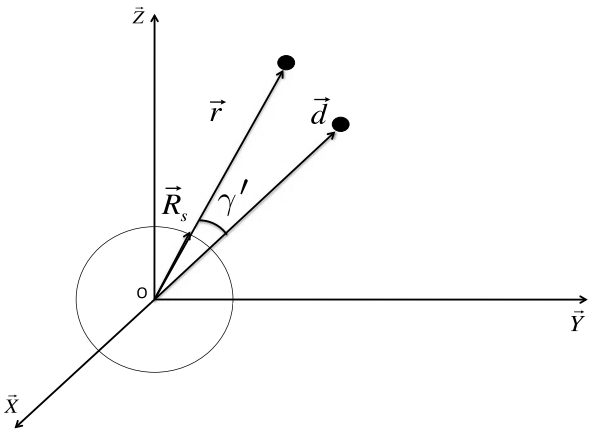

Fig. 5.2 Geometry of the tidal problem in the body reference frame $(\mathbf{e}_x, \mathbf{e}_y, \mathbf{e}_z)$. **d** is the vector pointing towards the disturbing body and **r** is the vector pointing towards the perturbed body. $\mathbf{R_s}$ targets at the surface of the body

implies that the satellite is elongated in the direction towards the planet and flattened in the perpendicular direction.

The tidal acceleration can be expressed through a tidal potential defined by

$$\mathbf{g}^T = \nabla U_T \tag{5.6}$$

where the tidal potential U_T is

$$U_T = \frac{GM_p}{2d^3}\left(2x_p^2 - y_p^2 - z_p^2\right) \tag{5.7}$$

in Cartesian coordinates, or

$$U_T = \frac{GM_p}{d}\left(\frac{R_s}{d}\right)^2 \frac{3\cos\gamma'^2 - 1}{2} \tag{5.8}$$

in spherical coordinates. The parameter γ' is the angle between the position vectors **d** and **x** as shown in Fig. 5.2. The last factor in the previous expression corresponds to the Legendre polynomial of degree 2, and the tidal potential is then written in synthetic form as

$$U_T = \frac{GM_p}{d}\left(\frac{R_s}{d}\right)^2 P_2\left(\cos\gamma'\right). \tag{5.9}$$

The Legendre polynomial of degree 2 results from the development performed in Eq. (5.3). The development at higher order in $|\mathbf{x}|$ leads to the introduction of higher degrees in the Legendre polynomial, and the generalized potential is then expressed as

$$U_T = \frac{GM_p}{d}\sum_{l=2}^{\infty}\left(\frac{R_s}{d}\right)^l P_l\left(\cos\gamma'\right). \tag{5.10}$$

The non-rigid satellite is distorted by the tidal potential. According to the degree-2 development in the potential, the satellite is elongated in two opposite directions. The resulting bulge follows the tidal acceleration and, in the case of an elastic body,

the bulge lies along the relative direction of the distorted satellite to the perturbing planet, as shown by Eq. (5.5). However, if the distorted material is not purely elastic, then the tidal bulge is offset with respect to the satellite–planet axis, i.e., the response of the material to stress is delayed as a consequence of internal friction. This phase lag with respect to the position of the tide-generating body induces dissipation inside the system, and the tidal bulge modifies the gravitational potential of the satellite. For small deformations a linear theory may be assumed, for which the tidal response of the distorted body is proportional to the external tidal potential evaluated at the surface. The coefficient of proportionality is called the dynamic Love number and it depends on the density and rheological structure of the body, and of the frequency of the excitation. Therefore, the dynamic Love number is different at each degree l, and the additional potential of the distorted satellite at a point $\mathbf{r}$ in space is then equal to

$$U = \frac{GM_p}{d} \sum_{l=2}^{+\infty} k_l \left(\frac{R_s}{r}\right)^{l+1} \left(\frac{R_s}{d}\right)^{l} P_l\left(\cos\gamma'\right) \tag{5.11}$$

(e.g. [29, 57]). The ratio $(R_s/r)^{(l+1)}$ comes from the Dirichlet theorem for external potential $r > R_s$. As a consequence, the external potential decreases quickly as a function of distance. For example, in the case of Miranda, the medium-sized satellite closest to Uranus, the ratio (R_s/r) is equal to 0.0018 and the error in the potential truncated at degree 2 is around 1/50. We then limit the description of the potential to the second degree; the simplified potential U is then

$$U = k_2 \frac{GM_p}{R_s} \left(\frac{R_s}{r}\right)^3 \left(\frac{R_s}{d}\right)^3 P_2\left(\cos\gamma'\right). \tag{5.12}$$

In this potential, the quantities $(R_s/d)^3, \gamma'$ are related to the tide-raising potential whereas the $(R_s/r)^3$ quantity represents the response of the satellite's potential at degree 2 (Eq. (5.11)).

In the case of a rigid homogeneous body, the Love number k_2 may be expressed as

$$k_2 = \frac{3/2}{1 + \frac{19\mu}{2\rho g R_s}} \tag{5.13}$$

where μ is the rigidity, ρ the density, g is the surface gravity acceleration, and R_s is the radius of the body. It is customary to introduce the dimensionless rigidity $\tilde{\mu}$

$$\tilde{\mu} = \frac{19\mu}{2\rho g R_s} \tag{5.14}$$

that represents the ratio of the elasticity to the cohesive force of the body's self-gravity. For small icy satellites the dimensionless rigidity $\tilde{\mu}$ is of the order of 10^2 and the rigidity dominates. The Love number can be thus simplified as

$$k_2 \sim \frac{3}{19} \frac{\rho g R_s}{\mu} \tag{5.15}$$

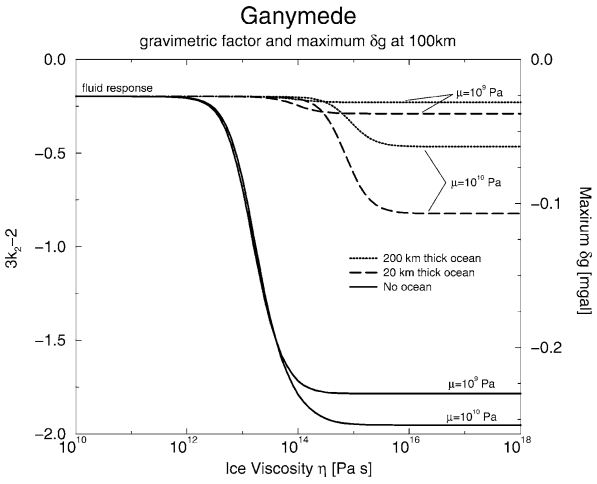

Fig. 5.3 Love number k_2 for different interior models assumed for Ganymede (from Moore and Schubert [76]). The *solid line* represents models without an internal ocean, whereas the thickness of the ocean is equal to 200 km (*dotted line*), and 20 km (*dashed line*). Each model is shown for two different assumptions on the value of the mean rigidity of the ice: $\mu = 10^9$ Pa and $\mu = 10^{10}$ Pa

whereas for a fluid body $\tilde{\mu}$ is equal to zero and the Love number is simply

$$k_2 = \frac{3}{2}. \tag{5.16}$$

However, most satellites are not homogeneous, with radial variations in composition and temperature (and also possibly in porosity in the smaller representatives). In this case, the Love numbers are smaller than the values predicted by Eqs. (5.15)–(5.16) and numerical integration is required to estimate these parameters (e.g. [13, 76, 112] and references therein). In addition, some large satellites like Europa, Ganymede, Callisto, and Titan might hold an internal ocean beneath their surface. In this case the tidal Love numbers increase toward the fluid limit as illustrated in Fig. 5.3 coming from Moore and Schubert [76].

When the tide-raising body located at **d** and the perturbed body disturbed by the potential **r** are the same, then **r** coincides with **d** in the elastic case. In the inelastic case, the vector **r** is out of phase with respect to **d** due to friction created by the motion of defects in the material. There are two main approaches for introducing into the equations the delay due to friction. The first approach proposed by Darwin [19, 20] and implemented by Kaula [57], Efroimsky and Williams [29], Ferraz-Mello et al. [31] is in four steps. (i) The tidal potential is developed in the form of Fourier series by expressing explicitly **r** and **d**, (ii) then, for each term of the series, a phase lag is introduced, and (iii) the gradient of the potential is computed with respect to the position of **r**, and finally (iv) **d** is replaced by **r**. This scheme is described and discussed in details in Efroimsky and Williams [29]. The phase lag ϵ is determined by the inelasticity of the body material and is a function of the forcing frequencies. The second approach is presented below in more details. This approach has the advantage to be simple, because the tidal lag is represented by a time delay Δt. This approach is however limited by the fact that the dissipation

factor, labeled Q, and the time delay Δt are linked through the following relationship that assumes that the object behaves like a Maxwell body, i.e.

$$\Delta t = (\omega Q)^{-1} \tag{5.17}$$

with ω is the synodic (or tidal) forcing frequency. However, according to laboratory measurements the frequency-dependence of the dissipation factor depends on the forcing frequency to the power α with α between 0.1 and 0.5 (see [67]). Keeping this limitation in mind, the lag is introduced by a Taylor development of $\mathbf{d} = \mathbf{r}(t - \Delta t)$ for each frequency, that leads to

$$\mathbf{d} \sim \mathbf{r}(t) - \Delta t \frac{d\mathbf{r}(t)}{dt}. \tag{5.18}$$

Therefore, $\mathbf{d}$ can be seen as the position of $\mathbf{r}(t)$ with a time delay Δt in the past relatively to the coordinate system linked to the body, and the tidal bulge is dragged by the rotation of the body.

The phase shift between the action and the response of the body leads to energy dissipation due to friction that can be expressed through the dissipation factor Q introduced in Eq. (5.17) [65]. The dissipation factor is defined as the maximum energy E stored during one cycle over the energy dissipated ΔE during that cycle [37]

$$Q = 2\pi \frac{E}{\Delta E}. \tag{5.19}$$

This definition is related to the damped harmonic oscillator model and the limitation of this analogy has been discussed in Greenberg [39] and Efroimsky and Williams [29].

The potential, Love number, and dissipation factor have been defined for a satellite deformed by a tide-raising planet. These expressions are still valid in the case of a planet deformed by a satellite by substituting all satellite parameters by planet parameters and the planet parameters by those corresponding to the tide-raising body (satellite or the Sun). However, in the case of giant planets, the power law equation (5.17) is not applicable because the full dynamics of the atmospheric response to the tide raising potential must be accounted for (e.g. [52]).

5.3 Tidal Dynamics

5.3.1 Introduction

Tidal interaction implies an evolution in the rotational motion and orbital parameters of satellites mainly due to the transfer of angular momentum between the satellite's orbit and planet's rotation as well as energy dissipation inside the satellite. The equilibrium configuration for an isolated two-body problem is a satellite in synchronous spin-orbit resonance and a circular orbit [87]. For a moon around the giant planet, the mutual gravitational interactions with the other satellites lead to equilibrium states close to this equilibrium configuration, as for example in the case of Io, for

which the Laplace resonance sustains a non-zero eccentricity and then a high dissipation regime as discussed below. Here we describe the tidal interaction between isolated body and we do not introduce the effect of the orbital resonances.

5.3.2 Transfer of Angular Momentum

The tidal potential generates a tidal bulge on the perturbed body. In the purely elastic case the tidal bulge is always aligned toward the perturbing body and, by symmetry, the resulting torque is null. Consequently, there is no transfer of angular momentum between the two bodies. In the inelastic case, the bulge is offset with respect to the direction between the satellite and the perturbing body and the resulting tidal torque drives an exchange of angular momentum.

A simple description of the angular momentum transfer can be investigated by considering a system composed of two rotating bodies, P and S, orbiting around a center of mass G, in circular orbit, and isolated in space. Here, we assume that P is a planet of mass M_p larger than the mass of the second body M_s, the satellite. The total angular momentum $\mathbf{H}$ of this system is the sum of the planet's angular momentum $\mathbf{H}_p$ and the satellite's angular momentum $\mathbf{H}_s$,

$$\mathbf{H} = \mathbf{H}_p + \mathbf{H}_s. \tag{5.20}$$

The planetary angular momentum is expressed in the barycentric reference frame of this system as

$$\mathbf{H}_p = M_p \mathbf{GP} \wedge \mathbf{v}_p + \mathbf{I}_p \boldsymbol{\Omega}_p \tag{5.21}$$

where $\mathbf{GP}$ is the direction vector between G and P, $\mathbf{v}_p$ is the orbital velocity of the planet around the center of mass, $\mathbf{I}_p$ the tensor of inertia of the planet, and $\boldsymbol{\Omega}_p$ its rotational velocity. Similarly, the angular momentum of the satellite is expressed as

$$\mathbf{H}_s = M_s \mathbf{GS} \wedge \mathbf{v}_s + \mathbf{I}_s \boldsymbol{\Omega}_s \tag{5.22}$$

where the indices s refer to the satellite. By using the barycenter definition of G, we simplify the expression of the total angular momentum as

$$\mathbf{H} = M_s \mathbf{PS} \wedge \mathbf{v}_s + \mathbf{I}_p \boldsymbol{\Omega}_p + \mathbf{I}_s \boldsymbol{\Omega}_s. \tag{5.23}$$

Consequently, the angular momentum is composed of the rotational angular momentum of each body with the satellite's orbital angular momentum around the planet but with the barycentric velocity. By assuming that the spins are normal to the orbital planes the vectorial equation is expressed as a scalar equation, where C_p and C_s are the polar moments of inertia of each body. In addition, for circular orbits, the velocity v_s can be simply expressed as $v_s = an$ with a the orbital radius and n the mean motion. Here we assume that the orbit of the satellite and the spin of the planet are rotating in the same sense. Triton is in a retrograde orbit, so v_s is then equal to $-an$. Table 5.2 presents physical parameters of the planets and satellites considered in this chapter. It appears that the rotational angular momenta of the planets and the

Table 5.2 Parameters of giant planets

Giant planet	Radius (km)	Mass (10^{24} kg)	P_{rot}
Jupiter	71398	1898.6	9h55m27.3s
Saturn	60330	568.46	10h39m22.4s
Uranus	26200	86.832	17.24 ± 0.01 h
Neptune	25225	102.43	16.11 ± 0.01 h

orbital angular momenta are much larger than the rotational angular momenta of the satellites by four to five orders of magnitude. Equation (5.23) is then simplified as

$$H = M_s a^2 n + C_p \Omega_p \tag{5.24}$$

that is a constant function of the motion for the isolated two body problem. This equation shows the relationship between the variation of the semi-major axis of the satellite (contained also in n through Kepler's third law) and the rotation of the planet.

To obtain the relationship between the semi-major axis and rotational rates, we derive Eq. (5.24),

$$M_s \frac{d(a^2 n)}{dt} + C_p \frac{d\Omega_p}{dt} = 0. \tag{5.25}$$

However, the derivation of the first term on the right-hand side is not straightforward, because a and n are related through Kepler's third law $n^2 a^3 = G(M_p + M_s) \simeq GM_p$. After introducing Kepler's third law and expressing n as a function of a, the variation of the semi-major axis a is directly related to the variation of the rotational velocity of the planet through

$$\frac{1}{a}\frac{da}{dt} = -2\frac{C_p}{M_p R_p^2}\left(\frac{M_p}{M_s}\right)\left(\frac{R_p}{a}\right)^2 \frac{1}{n}\frac{d\Omega_p}{dt} \tag{5.26}$$

or

$$\frac{da}{dt} \propto -a^{1/2}\frac{d\Omega_p}{dt}. \tag{5.27}$$

The satellite's semi-major axis and the planet's angular velocity evolve in opposite directions, that is the planet's angular velocity decreases if the satellite's orbit expands, and vice-versa due to the transfer of angular momentum between the orbit and the rotation. In the case of Triton, which is in retrograde orbit, the sign of the right-hand side is positive meaning that acceleration in the spin corresponds to an expansion of the orbit, and deceleration in the spin implies a contraction of the orbit. The evolution of the Triton dynamics is described in Correia [18].

The variation in the planet's angular velocity can be computed from the gravitational torque exerted by the satellite on the offset planetary bulge. The rotational $\mathbf{H}_p^R$ angular momentum of the planet is equal to the torque applied to the planet

$$\frac{d\mathbf{H}_p^R}{dt} = \mathbf{T}. \tag{5.28}$$

As $H_p^R = C_p \Omega_p$, under the assumption that the spin vector is aligned along the polar axis $\mathbf{e}_z$ and C_p is assumed to be constant, we have

$$\frac{d\Omega_p}{dt} = \frac{1}{C_p} T_z. \tag{5.29}$$

The vectorial torque is the cross-product of the radial vector between the centers of mass of the planet and of the satellite with the tidal force resulting from the tidal potential ∇U expressed in Eq. (5.12):

$$\frac{d\Omega_p}{dt} = \frac{M_s}{C_p} (\mathbf{r} \wedge \nabla U)_z. \tag{5.30}$$

By using the potential equation (5.12) and Q defined in Eq. (5.17), we obtain the relation

$$\frac{d\Omega_p}{dt} = -\frac{3}{2} \left(\frac{k_2}{Q} \right)_p \frac{G M_s^2 R_p^5}{C_p a^6} \text{sign}(\Omega_p - n) \tag{5.31}$$

where the sign represents the effect of the torque braking the spin of the planet and leading to spin synchronization (because here the orbit is assumed to be circular). Combining Eqs. (5.26) and (5.31) with $\Omega_p > n$, we obtain the final expression of the evolution of the orbital motion of the satellite due to the tides raised in the planet (e.g. [37]):

$$\frac{da}{dt} = +3 \left(\frac{k_2}{Q} \right)_p \frac{M_s}{M_p} \left(\frac{R_p}{a} \right)^5 na, \tag{5.32}$$

or

$$\frac{da}{dt} \propto \left(\frac{k_2}{Q} \right)_p a^{-11/2}. \tag{5.33}$$

So far these equations have been developed for a circular orbit. If the eccentricity is non-zero, the tides raised by the satellites on the planets increase the orbital eccentricity of the satellite as shown by Jeffreys [55], Goldreich [35]. By expanding the tidal potential U, Eq. (5.12), in Fourier series and then working out the equations of orbital element variations, the evolution of the eccentricity is derived as [37]

$$\frac{de}{dt} = +\frac{57}{8} \left(\frac{k_2}{Q} \right)_p \frac{m_s}{m_p} \left(\frac{R_p}{a} \right)^5 ne. \tag{5.34}$$

The effect is to increase the eccentricity because for almost satellites we are in the case where $\Omega_p > n$, i.e., outside the synchronous orbit (where $\Omega_p = n$). In this case, the impulse due to the planetary tidal bulge on the satellite is larger at the periapsis, increasing the apoapses distance and then the eccentricity.

5.3.3 Tides Raised on the Satellites

5.3.3.1 Introduction

The consequences of the tides acting on the planet have been described in the previous section and now we tackle the question of the tides acting on the satellites.

These drive despinning and generally lead to synchronization of the satellite's rotation with its orbital motion in a time shorter than the age of the solar system. Besides, the orientation of the satellite's spin converges toward an equilibrium value called the *Cassini state* that is generally close to the normal to the orbital plane ([10, 17]; see review in [18, 87]).

Exceptions are Phoebe and Nereid that are too far from their parent-planets, more than 200 planetary radii (Table 5.1). Also, Hyperion stands out as the only satellite presenting a chaotic rotation due to its strong non-spherical shape [120].

Other consequences of the tides raised on the satellites include circularization of the orbits and contraction or expansion of the semi-major axes, depending on the relative amounts of dissipation inside the planet and in the satellite and if orbital resonances are present [87].

5.3.3.2 Despinning

The initial spin rate of the main satellites is estimated to be a few hours (e.g. [87]). However, at present time most satellites are rotating synchronously (see Table 5.1). Spin rate evolution is the consequence of the tides raised in the satellite by the parent-planet gravitational potential. This torque may be computed from Eq. (5.31), in which the orbit of the satellite is assumed to be circular, in the equatorial plane of parent-planet, and the obliquity is equal to zero (e.g. [31, 35, 65])

$$\Gamma = \frac{3}{2}\left(\frac{k_2}{Q}\right)_s \frac{GM_p^2}{R_s}\left(\frac{R_s}{a}\right)^6 \text{sign}(\Omega_s - n). \tag{5.35}$$

This torque acts to despin the satellites on a relatively short timescale, of a few million years. The evolution of the angular momentum yields

$$\frac{dC_s\Omega_s}{dt} = \Gamma \tag{5.36}$$

and

$$\frac{d\Omega_s}{dt} = -\frac{3}{2}\left(\frac{k_2}{Q}\right)_s \frac{GM_p^2 R_s^5}{C_s a^6}\text{sign}(\Omega_s - n) \tag{5.37}$$

and by introducing the Love number defined in Eq. (5.15)

$$\frac{d\Omega_s}{dt} = -\frac{45}{76}\left(\frac{\rho_s R_s^2}{\mu_s Q_s}\right) n^4 \text{sign}(\Omega_s - n). \tag{5.38}$$

The damping timescale is then estimated to be equal to [87]

$$\tau \approx \frac{76}{45}\left(\frac{\Omega_s \mu_s Q_s}{\rho_s R_s^2}\right)\frac{1}{n^4}. \tag{5.39}$$

Here, Q_s is the dissipation factor, C_s the polar moment of inertia, ρ_s the mean density, and μ_s the mean bulk modulus of the satellite. For typical values of $Q_s = 100$ and $\mu_s = 10^{10}$ Pa, we infer from Eq. (5.39) that the despinning timescale decreases

when the satellite's size increases. After the tidal modeling of MacDonald [65] the resulting satellite despinning time is around a few million years, except for the distant Iapetus whose despinning timescale is of the order of the age of the solar system due to the large distance from Saturn [1]. However, more realistic models of dissipation gives for Iapetus a despinning time around 0.9 Gyr [13]. This leads to the general observation that the consequences of tidally-induced stressing may significantly vary from one modeling framework to another, and this is particularly the case for the MacDonald approach and the more elaborate modeling developed by Efroimsky and Williams [29] or Ferraz-Mello et al. [31] based after [19, 20].

In the case of a circular orbit, the final spin state is at the exact synchronous resonance. However, if the orbit is eccentric the final rotational period is slightly larger than the orbital period. For the tidal model based on [65] the spin frequency is expressed as [63, 119]

$$\Omega_s^e = n\left(1 + \frac{19}{2}e^2\right). \tag{5.40}$$

The spin frequency is larger than the orbital frequency, because the tidal torque is larger at the periapsis and leads to a positive torque on the satellite that accelerates its spin rate.

5.3.3.3 Spin-Orbit Resonance

Most large satellites are in synchronous resonance with a non-zero eccentricity. The mechanism leading to the capture of the satellites in spin-orbit resonance is the gravitational torque exerted by the parent-planet on the asymmetrical shapes of the satellites. Therefore Eq. (5.36) becomes

$$\frac{dC_s\Omega_s}{dt} + \frac{3}{2}\left(\frac{a}{d}\right)^3 n^2(B_s - A_s)\sin 2\gamma = \Gamma \tag{5.41}$$

where the second term on the left-hand side represents the restoring torque. The angle γ is the orientation of the satellite's long axis relative to the direction of the satellite to the planet (e.g. [36]). The stability criterion for capture into resonance is that the average tidal torque must be smaller than the maximum possible restoring torque due to the parent-planet [36]. This is expressed as

$$\left|\langle\Gamma\rangle\right| < \frac{3}{2}(B_s - A_s)n^2\left(\frac{a}{d}\right)^3. \tag{5.42}$$

By using the expression of the tidal torque equation (5.35) and for a small eccentricity, we obtain the constraint on the triaxiality of the satellite $(B - A)/C$ for synchronization to occur:

$$\frac{B_s - A_s}{C_s} > \frac{1}{C_s}\left(\frac{k_2}{Q}\right)_s \frac{R_s^5}{G}. \tag{5.43}$$

Therefore if the permanent asymmetrical bulge $(B_s - A_s)$ is large enough the satellite can be captured into synchronous resonance. It appears that for most satellites the hydrostatic value of $(B_s - A_s)$ (Sect. 5.4) is always larger than the critical value, implying systematic capture in resonance, as observed in nature. However, the direction of the long axis of the satellite is slightly shifted from zero at the pericenter because of the balance between the non-zero tidal torque and the permanent torque [123]. That offset in the direction of the satellite is relatively small. For example, in the case of Enceladus the shift is estimated at a maximum 0.57 degrees [92]. Measuring such a small displacement is challenging, even with an orbiter, but the required measurement accuracy may be achieved with an in situ tracking device, such as a transponder. In addition, it has been suggested that a transient regime may occur. Indeed, since the figure axis is shifted, the shape of the satellite may relax by creep in order to adjust to the external potential resulting in the satellite's rotating slightly faster than the synchronous rotation to maintain an equilibrium orientation, and implying a non-synchronous motion of the surface [41, 121]. While there is no direct evidence for such a motion from *Voyager* and *Galileo* images, the interpretation of tidally-induced tectonic patterns at Europa seems to support this scenario ([42], [44, Sect. 5.5.5]).

5.3.3.4 Satellite Orbital Evolution

The rotational equilibrium configuration of most satellites is the synchronous spin-orbit rotation regime, since the despinning time is generally shorter than the age of the solar system. In this case, on average, the tidal bulge of the satellite is aligned with the gravitational force of the planet. As a consequence, there is no transfer of angular momentum between the satellite's orbit and rotation. However, if the satellite has a non-zero orbital eccentricity, it is deformed more strongly at the periapsis than at the apoapsis leading to a time-varying tidal potential called *radial tides*. In addition, the long-axis of the satellite oscillates around its mean value because the velocity of the orbital motion varies along the elliptical orbit [79]: it accelerates at the periapsis and decelerates at the apoapsis according to Kepler's second law. This oscillation is called the optical libration. Its amplitude is equal to twice the eccentricity, and it leads to a second time-varying potential term called *librational tides*. Due to the radial and librational tides, the orbital energy is still transferred between the satellite's orbit and rotation, which affects the satellite's orbit over long timescales [35].

Here, the energy source is the orbital energy $-GM_sM_p/2a$ whose dampening by the tidal dissipation decreases the semi-major axis. As the orbit angular momentum $M_s n a^2 \sqrt{1-e^2}$ is conserved, the decrease in the semi-major axis a is associated with a decrease in the eccentricity e leading to the circularization of the orbit. The temporal evolution of the semi-major axis and eccentricity have been expressed by Goldreich and Soter [37] for a satellite not involved in any orbital resonance:

$$\frac{da}{dt} = -21\left(\frac{k_2}{Q}\right)_s \frac{m_p}{m_s}\left(\frac{R_s}{a}\right)^5 nae^2, \tag{5.44}$$

$$\frac{de}{dt} = -\frac{21}{2}\left(\frac{k_2}{Q}\right)_s \frac{m_p}{m_s}\left(\frac{R_s}{a}\right)^5 ne. \tag{5.45}$$

We note that the semi-major axis and eccentricity evolution rates are negative leading to a decrease of both quantities as long as the eccentricity is non-zero. As the evolution of the eccentricity is faster than the evolution of the semi-major axis (which depends on e^2), the orbit is circularized well before the semi-major axis a is significantly modified.

The combined evolution of the semi-major and eccentricity result in the combination of the tides raised on the planet, Eqs. (5.32) and (5.34), and the tides raised on the satellite, Eqs. (5.44) and (5.45) for satellites outside orbital resonances. The tides raised on the satellites lead to a decrease in both the semi-major axis and eccentricity, whereas the tides raised on the planet lead to an increase of both quantities, since all major satellites of the giant planets evolve beyond the synchronous orbit (defined by the distance to the primary at which the orbital period equals the rotation period of the planet, $\Omega_p = n$). The orbital evolution of the satellites around the same parent-planet depends on their semi-major axes, sizes, material properties, and thermal evolution. Consequently, the satellites cross many orbital resonances, as for example Dione and Enceladus that are currently in 2:1 resonance or the Galilean satellites, Io, Europa, Ganymede, that are in 4:2:1 resonance (the *Laplace resonance* discussed in more details below). Resonance crossing leads to an additional transfer of angular momentum (e.g. [71]) that strongly influences the orbital evolution of the satellites. In addition, when the satellites are in orbital resonances, eccentricity pumping prevails over the circularization of the orbit, which further sustains tidal heating inside the satellites as discussed in Sect. 5.5.

Tidal dissipation also affects the inclinations of the satellites orbits. The equilibrium configuration depends on the distance of the moon to the parent-planet [87]. If a moon is close to its planet, the orbital precession is mainly driven by the oblateness of the planet, and the equilibrium orbital plane coincides with the equatorial plane of the planet. This is the case for the majority of the satellites and thus explains why these objects have a small inclination (usually around 1 degree or less). On the other hand, if the moon is far from its planet, the orbital precession may be dominated by the action of the Sun, in which case the equilibrium orbital plane coincides with the mean orbital plane of the planet (i.e. the orbital plane of the Sun seen from the planet). In the intermediate position, the equilibrium plane is between the equatorial and orbital planetary planes, as seen for example in the case of Iapetus [117].

5.3.3.5 Measurements of Tidal Accelerations

Measurement of the dissipation in giant planet systems through the tracking of natural satellite orbital motion started about one century ago with de Sitter [24]. The

method consists in fitting astrometric measurements of the satellites positions observed over long periods with orbital model including the tides. However, assessing the influence of the tides on the orbital motions of the satellites is complex because the satellites orbits are perturbed by mutual gravitational attraction with other satellites as well as by the non-spherical shape of the parent-planet. Consequently, the determination of the tides requires accurate numerical models that account for the many dynamical perturbations expected over long duration observations, in order to decorrelate the various dynamical effects (long periods with secular effects due to the tides). Such studies have been performed by Lainey et al. [61, 62] on the Galilean and Saturnian satellites.

For the Galilean system, the accelerations due to the tides have induced a cumulative shift in the satellite orbital positions of 55 km, −125 km and −365 km for Io, Europa, and Ganymede, respectively over the past 116 years analyzed by Lainey et al. [61]. This means that Io's orbit is contracting, while the orbits of Europa and Ganymede are expanding.

The orbital motions of Io, Europa, and Ganymede are driven by the Laplace resonance, i.e. their mean motions are related through (e.g. [40]):

$$n_1 - 3n_2 + 2n_3 = 0 \tag{5.46}$$

where 1, 2, 3 correspond to Io, Europa, and Ganymede, respectively and n is the mean motion. This resonance results in the excitation of the satellites eccentricities and is thus instrumental in maintaining significant tidal dissipation in Io and Europa. However, since these satellites are evolving in opposite directions, it is expected that they would eventually escape from the Laplace resonance [61, 97].

In addition, from the determination of the semi-major axis evolution of these satellites Lainey et al. [61] could infer the ratios k_2/Q characteristic of Jupiter and Io. The relationship between the semi-major axis and the eccentricity evolution rates with k_2/Q are shown in Eqs. (5.32), (5.34), (5.44), and (5.45). The tides within Europa and Ganymede are not measurable because of the orbital correlations caused by the Laplace resonance. The tides related to Callisto are negligible because the satellite is too far from Jupiter ($H = 89.2$ meters for Callisto whereas it is 3119 meters for Io, see Table 5.1). The k_2/Q ratio for Io is then equal to 0.015 ± 0.003, which is consistent with the value inferred from heat flow mapping. Such a result implies that Io's interior is close to thermal equilibrium and that the heat flow radiated at the surface is mainly due to tidal heating [61].

Jupiter's k_2/Q is equal to $(1.102 \pm 0.203) \times 10^{-5}$ [61]. On top of this, geophysical model of Jupiter's interior that yields the value of k_2 leads to the determination of Jupiter's dissipation factor. Gavrilov and Zharkov [34] predicted a value of 0.379 implying a Q factor of $(3.56 \pm 0.66) \times 10^4$. This value is close to the lower bound on Q determined from the tidally-induced orbital migration of the satellites over the age of the solar system that is in the range $6 \times 10^4 < Q < 2 \times 10^6$ [123]. The dissipation determined by Lainey et al. [61] is consistent with the dissipation models of Jupiter. This result shows that dissipation within giant planets is much stronger than anticipated for the past four decades.

A similar study performed by Lainey et al. [62] for the Saturnian system lead to the determination of Saturn's (k_2/Q) equal to $(2.3 \pm 0.7) \times 10^{-4}$. This value is one

order smaller (so larger dissipation) than the usual value estimated from theoretical arguments [83]. In addition, Lainey et al. [62] found that the orbit of Mimas moves toward Saturn at a rate of $da/dt = -(15.7 \pm 4.4) \times 10^{-15}$ au/days. It is not possible to derive directly Mimas' k_2/Q from that rate as was done for Io because the satellite is in resonance with Tethys and also interacts with the Saturnian rings.

The measurement of the tides expressed in the Saturnian system brings new information on the understanding of this system. For example, Enceladus presents plumes and heat emerging from the south pole. The associated energy is estimated to be about 15.8 ± 3.1 GW [45]. Meyer and Wisdom [71] using an obsolete ancient determination of Saturn's k_2/Q pointed out that this power can not be produced from tidal dissipation because it is then inconsistent with the long-term preservation of Enceladus' eccentricity [71]. However, by taking into account the additional transfer of angular momentum resulting from the 2:1 resonance with Dione [71] and the new k_2/Q value, Lainey et al. [62] explained both the observed heat and the preservation of Enceladus' eccentricity. In addition, in that framework, Saturn's dissipation factor is inconsistent with the scenario assuming that the moons formed outside the synchronous orbit and then migrated to their current positions. A recent model of accretion of the moons inside and at the outer edge of Saturn's rings appears more consistent with the observed dissipation as well as geological observations and satellite surface composition [14, 62].

In summary, astrometric measurements have led to a quantification of the dissipation inside Jupiter and Saturn by combining accurate modern numerical models and a historical astrometric record spanning more than one century. The dissipation in the Uranian and Neptunian systems has not been estimated at this time. The strong correlation due to the Laplace resonance makes it more difficult to infer the tidal dissipation in Europa and thus complementary methods are required to determine that parameter, for example, through accurate characterization of the satellite's rotation, as shown by Rambaux et al. [92] for Enceladus, or by direct measurement of the gravity field and surface displacement [116]. Both of these techniques require in situ observations, with a dedicated orbiter or surface tracking instruments (e.g. beacons, very broad-band seismometer).

5.4 Static Tides and the Shape of the Moons

5.4.1 Introduction

The secular shapes of major satellites in synchronous rotation can be well approximated by a triaxial ellipsoid under the assumption of hydrostatic equilibrium [6, 21, 125]. This shape results from the deformation of the body in response to the centrifugal and tidal forces. The tidal force acts to elongate the moon along the parent-planet-satellite direction. This is due to the synchronous resonance as the satellites keep the same face towards the parent-planet. The centrifugal force acts to flatten the satellite's shape along its rotation axis. The combination of these two

forces leads to a triaxial shape because the parent-planet generating the tidal force is usually in the equatorial plane of the satellite. The amplitude of the resulting distortion depends on distribution of mass inside the body. Hence shape data can be used to obtain information on the interior.

In practice, the forces shaping the satellites present a secular and a periodic component. The consequences of the periodic component are discussed in the next section. Here, we focus on the time-independent (secular) contribution of the forces and the resulting equilibrium shape of the satellite, i.e., when the satellite's shape had time to relax to an equilibrium ellipsoid with the long axis pointing toward the parent-planet and the short axis aligned with the rotating axis.

The steady rotational potential determining the equilibrium shape is

$$U_c = \frac{\Omega_s^2 r^2}{3}\big(P_{20}(\cos\theta) - 1\big) \tag{5.47}$$

where the potential acts at a point located at (r, θ, λ) with r the radial component, θ the colatitude, and λ the longitude. The parameter P_{20} is the Legendre polynomial at degree 2 and order 0. Due to the axial symmetry, the potential is independent from the longitude λ. Ω_s is the mean angular rotation of the satellite and is equal to the mean motion due to the synchronous rotation. The tidal potential is expressed in spherical coordinates as in Eq. (5.8) that we recall here

$$U_T = \frac{GM_p}{d}\left(\frac{R_s}{d}\right)^2 \frac{3\cos^2\gamma' - 1}{2}. \tag{5.48}$$

Here, the tidal potential contains both a secular and a periodic component in the development of the radial distance d and in the orientation angle γ'. The secular part in d is obtained by assuming that the orbit of the satellite is circular; the secular part of the orientation is evaluated for an equatorial orbit and assuming that the moon is in exact spin-orbit synchronous rotation. Thus the angle γ' is expressed by

$$\cos\gamma' = \sin\theta\cos\lambda. \tag{5.49}$$

Combining the centrifugal and tidal potentials results in

$$\phi_2 = \Omega_s^2 R_s^2\left(-\frac{5}{6}P_{20}(\cos\theta) + \frac{1}{4}P_{22}(\cos\theta)\cos 2\lambda\right). \tag{5.50}$$

5.4.2 Moments of Inertia

The secular potential equation (5.50) entails a permanent deformation of the satellite. The induced potential at the surface R_s of the satellite is assumed to be linear in ϕ_2 with a coefficient of proportionality, the secular Love number labeled here as k_f:

$$\delta\phi_2 = k_f\phi_2. \tag{5.51}$$

The secular Love number is equal to 3/2 for a homogeneous body in hydrostatic equilibrium. Its value decreases as density increases with depth (see Sect. 5.2).

The response of the satellite to the secular potential induces a potential that can be developed in spherical harmonics to degree 2 as:

$$\delta\phi_2 = \frac{GM}{a}\sum_{n=0}^{\infty}\left(\frac{a}{r}\right)^{n+1}\sum_{m=0}^{n}(C_{n,m}\cos m\lambda + S_{n,m}\sin m\lambda)P_{n,m}(\sin\varphi) \tag{5.52}$$

and the identification between the potential equations (5.51) and (5.52) of each degree-2 term leads to the relation

$$C_{20} = -\frac{5}{6}k_f q \tag{5.53}$$

$$C_{22} = \frac{1}{4}k_f q, \tag{5.54}$$

where we have introduced the dimensionless parameter $q = \frac{\Omega_s^2 R_s^3}{GM_s}$ corresponding to the ratio of the centrifugal to the gravitational potential at the equator. The C_{22} coefficient is a purely tidal term, whereas C_{20} can be decomposed into a component induced by the centrifugal potential (1/3) and another one from the tidal potential (1/2). The relations (5.53) and (5.54) can be simply combined as

$$C_{20} = -\frac{10}{3}C_{22}. \tag{5.55}$$

As noticed by Moore et al. [77], this relation indicates that the body responds to the sum of the time-averaged centrifugal and tidal potentials and there is no additional deviation from spherical symmetry. This relation is often shortly assimilated as a consequence of the hydrostatic equilibrium. However, in order to assess the equilibrium state of the object it is necessary to compare its shape and gravity data, as discussed in more details below.

If the body is in hydrostatic equilibrium, another step toward understanding its interior comes from the Radau-Darwin approximation. The gravitational coefficients C_{20} and C_{22} are related to the satellite's principal moments of inertia A, B, C (with $C > B > A$) through [122]

$$C_{20} = -\frac{2C - (B + A)}{2MR^2}, \tag{5.56}$$

$$C_{22} = \frac{B - A}{4MR^2} \tag{5.57}$$

and the axial moment of inertia C/MR^2 can be deduced from the Radau-Darwin approximation for hydrostatic bodies [79]:

$$\frac{C}{MR^2} = \frac{2}{3}\left[1 - \frac{2}{5}\left(\frac{4 - k_f}{1 + k_f}\right)^{1/2}\right]. \tag{5.58}$$

In theory, the inferred moment of inertia is a simple function of the internal mass distribution inside an object.

In practice, satellites shapes and interiors depart from hydrostaticity due to mass concentrations, large variations in topography at various scales, or even sometimes a fossil bulge relic of an earlier stage in the evolution of the object. That bulge may

be acquired before a moon became locked in spin-orbit resonance or during the tidal migration of the satellite. A famous example is Saturn's satellite Iapetus that presents a large equatorial bulge frozen when the object had a rotation period of 16 hours that strongly differs from its current 80 day rotation period [12]. In the case of endogenic sources of non-hydrostaticity (e.g. mass anomalies, stress associated with internal activity, such as convection) the impact on the gravity and shape is expressed at degrees higher than two [33].

5.4.3 Satellite Shapes

Under the assumption of hydrostatic equilibrium the shapes of synchronous satellites may be approximated as triaxial ellipsoids with principal axes denoted (a, b, c), where a is the long axis pointing toward the parent-planet, c the short axis along the polar axis, and b the intermediate (equatorial) axis. The proportional factor between the excitation and the radial response of the satellite is determined by the fluid Love number, h_f, defined as [78, 116]

$$u = h_f \frac{\phi_2}{g} \tag{5.59}$$

where u is the vertical tidal surface displacement and g is the gravitational acceleration at the satellite's surface. If the body is in hydrostatic equilibrium, then h_f is related to k_f by the following relationship (e.g. [125])

$$h_f = k_f + 1. \tag{5.60}$$

Therefore, a strengthless and homogeneous body is characterized by k_f equal to $3/2$ and h_f to $5/2$. As for k_f, the Love number h_f depends on the density profile. Departure from the equality (5.60) implies that the object is not in hydrostatic equilibrium, a crucial piece of information on the evolution of the object. Indeed, the ability of an object's shape to relax or to preserve non-hydrostatic anomalies over the long term is a function of the maximum temperature reached within the object and the mechanism driving heat transfer.

The Love number h_f may be deduced from the principal axes of the ellipsoid through [22, 125]

$$a = R_s\left(1 + \frac{7}{6}qh_f\right), \tag{5.61}$$

$$b = R_s\left(1 - \frac{1}{3}qh_f\right), \tag{5.62}$$

$$c = R_s\left(1 - \frac{5}{6}qh_f\right) \tag{5.63}$$

neglecting terms of order 2 in q. Thus, by determining k_f from gravity data, it is possible to estimate the principal axis of a given satellite in hydrostatic equilibrium. Comparison with actual shape data, if available, leads to constraints on the departure

of hydrostaticity of the object and then on its internal and surface evolution. In addition, these relations imply that

$$(a - c) = 4(b - c) \tag{5.64}$$

assuming that higher orders in the parameter q can be neglected.

5.4.4 Gravity and Shape Observations

5.4.4.1 Observational Methods

The gravity field of a satellite is measured by accurately tracking the trajectory of a spacecraft approaching the object and accounting for orbital perturbations acting on the spacecraft. Accurate measurement of the spacecraft's position is inferred from the shift in the radio signal Doppler frequency tracked from Earth's ground stations. The requirement in the accuracy of the Doppler shift is a few hundred meters per second.

The determination of the gravity field, and especially the C_{20} and C_{22} coefficients, requires enough flybys distributed in equatorial and polar orbits in order to determine each coefficient independently and verify whether the hydrostaticity assumption (5.55) applies to the object. When the gravity data are too sparse, it is still possible to determine the gravity field by assuming the relation (5.55). Such approach imposes a strong constraint on the geophysics of these bodies that has to be kept in mind during the interpretation of the data. The gravity data reduction technique is described in [98] review on the Galilean satellites, and in [60] for the Saturnian satellites.

The global shape of a satellite is determined by combining the various limb profiles of wide-angle images and then searching for an ellipsoid that can match these observations [22, 109, 110], or by using an altimeter such as *Cassini*'s RADAR altimeter for Titan [124]. The gravity and topography fields can be combined to infer constraints on the interior, such as non-hydrostatic anomalies. However, shape and gravity observations have been obtained only for a few bodies: Io, Europa, Ganymede, Callisto by the *Galileo* spacecraft and Enceladus, Rhea, and Titan by the *Cassini* spacecraft (see Table 5.3).

5.4.4.2 Galilean Satellites

The density of Io is relatively high (3.530 $\mathrm{g\,cm^{-3}}$) indicating that this satellite is primarily rocky. Europa also presents a high density 3.013 $\mathrm{g\,cm^{-3}}$ but its surface is totally covered with ice, suggesting the presence at depth of a large rocky core. Ganymede and Callisto have lower densities consistent with an ice mass fraction around 30 %. Magnetometer data suggest that the three icy satellites shelter deep oceans beneath their icy surfaces [98]. This hypothesis is also supported by the

Table 5.3 Gravity data provided by the *Galileo* (a) and *Cassini* (b) missions. (a) Schubert et al. [98], (b) MacKenzie et al. [66]. Rhea is not in hydrostatic equilibrium and the Radau-Darwin approximation can not be applied, (c) Iess et al. [53]. The data for the gravity field of Enceladus are not available at this time

Satellites	$C_{20}(10^{-6})$	$C_{22}(10^{-6})$	C/MR^2	k_f
Io$^{(a)}$	-1859.5 ± 2.7	558 ± 0.8	0.37824 ± 0.00022	1.3043 ± 0.0019
Europa$^{(a)}$	-435.5 ± 8.2	131.5 ± 2.5	0.346 ± 0.005	1.048 ± 0.0020
Ganymede$^{(a)}$	-12753 ± 2.9	38.26 ± 0.87	0.3115 ± 0.0028	0.804 ± 0.018
Callisto$^{(a)}$	-32.7 ± 0.8	10.2 ± 0.3	0.3549 ± 0.0042	1.103 ± 0.035
Rhea$^{(b)}$	-931 ± 12	237.0 ± 4.5	–	–
Titan$^{(c)}$	-31.808 ± 0.404	9.983 ± 0.039	0.3414 ± 0.0005	1.0097 ± 0.0039

geological record and can be explained by thermal evolution models ([9, 49, 59, 86, 98] and references therein).

The gravity fields of the Galilean satellites have been determined during the *Galileo* mission that dedicated 4–5 flybys to each satellite (see a review in [98]). As *Galileo* performed 4 equatorial flybys and 1 polar flyby of Io, Anderson et al. [4] managed to decorrelate the C_{20} from the C_{22} coefficients. In the case of Ganymede even with the equatorial and orbital flybys [2], it is not possible to decorrelate the two coefficients and the relationship (5.55) has to be assumed [98]. Indeed, the gravity field of Ganymede includes components of degree and order 4 due to mass concentration that could be detected by disk-cap mass anomaly modeling [85]. The situation is even worse in the case of Europa and Callisto because the gravity passes at these objects where all in near equatorial orbit, so that only C_{22} could be determined [3, 5]. However, the gravity field of Callisto presents a non-zero S_{22} coefficient suggesting that an anomaly (interior, surface) may affect its potential [5].

At first order, the shape data available for the Galilean satellites are mostly consistent with ellipsoids in hydrostatic equilibrium [5, 98]. As a consequence, constraints on the density profile may be obtained from inferring the secular Love number k_f from C_{22} through Eq. (5.54) and the Radau-Darwin equation (5.58). Results displayed in Table 5.3 indicate that the satellites are not homogeneous because their C/MR^2 values are smaller than 0.4, i.e. the upper limit corresponding to a homogeneous spherical body. Models of these satellites matching both their axial moments of inertia C/MR^2 and mean densities indicate that Io, Europa, and Ganymede present a core enriched in rock, while Callisto is partially differentiated ([98] and references therein).

5.4.4.3 Saturnian Satellites

The gravity and topography of the Saturnian satellites have been inferred from observations obtained by the *Cassini-Huygens* mission that arrived in the system on July 1st, 2004. The *Cassini* orbiter performed several flybys of all major satellites

but only a few of these flybys have been dedicated to radio science tracking that enables gravity field measurement. So far, only the gravity fields of Titan, Enceladus, and Rhea have been obtained to degree two. For the other medium-sized satellites, only the mass has been determined from radio tracking of *Cassini*, so far (see a review in [60]).

Titan has a particular place in the family of the Saturnian satellites. It is the largest with a radius of 2575 km, i.e. 3.4 times the radius of Rhea (764 km) and it is the only moon with a thick atmosphere, which is composed mainly of Nitrogen and Methane. This thick atmosphere precludes the direct observation of Titan's surface, and only Cassini RADAR, VIMS (Visual and Infrared Mapping Spectrometer), and the in-situ *Huygens* probe that revealed a fascinating world revolving around rich geological features such as dunes, channels, lakes, impact craters, and putative cryovolcanos. The gravity and topography measurements bring constraints on Titan's interior, which will help assess the relative contribution of endogenic activity and atmospheric processes to the evolution of the surface.

The gravity field of Titan has been determined by Iess et al. [53] based on four dedicated gravity science flybys by *Cassini*. In an earlier study based on 3 flybys, Rappaport et al. [94] inferred the gravity field to degree two and found the ratio of C_{20}/C_{22} to be different from the $-10/3$ value expected for an object in hydrostatic equilibrium. However, by using one more flyby and introducing the degree 3 coefficients, Iess et al. [53] inferred C_{20}/C_{22} around $-10/3$, hence demonstrating the importance of including higher degree terms in the inversion of gravity data. So Titan's quadrupole field is consistent with that expected for a hydrostatically relaxed body shaped by tidal and rotational potentials. By applying the Radau-Darwin approximation, Iess et al. inferred Titan's polar moment of inertia C/MR^2 equal to 0.3414 ± 0.0005. This information, combined with the mean density, is an important constraint on interior models. The relatively large value of Titan's C/MR^2 (as a reference, Ganymede's mean moment of inertia is equal to ~ 0.3115 [98]) suggests that it is only partially differentiated, and that its core may contain a large fraction of water, either in the form of ice mixed with rock [7] or as water of hydration, i.e. water trapped in the silicate structure [11, 32].

In addition, the topography of Titan has been measured by radar altimetry data [124]. These authors determined a ratio of $(a-c)/(b-c) \approx 2.2$ that differs from the hydrostatic equilibrium inferred by [53] from their gravity data under the assumption of hydrostatic equilibrium. Thus Titan appears more flattened than predicted for a hydrostatically relaxed body. Nimmo and Bills [81] suggested that the discrepancy could be related to large lateral variations in the icy shell thickness. Choukroun and Sotin [15] showed that this difference might be imputed to meteorological and chemical processes acting on the icy surface as part of a methane-ethane substitution cycle. Therefore, this result highlights the importance of clearly separating the hydrostatic contribution of the shape resulting from the secular tidal potential in order to quantify the non-hydrostatic contributions due, in this case, to atmospheric processes.

Another Saturnian satellite of major interest is Enceladus, due to its active south polar region that may be associated with a liquid water reservoir [91, 106]. Only

three gravity passes have been dedicated to Enceladus. While the results are not available at this time, the preliminary data indicate that the gravity field of Enceladus contains a non-negligible degree-three component [26]. These authors reported that the degree 2 coefficients dominate, as expected for a synchronous satellite, but the C_{20} and C_{22} present a small departure from the values predicted under the assumption of hydrostatic equilibrium. In addition, the C_{30} is negative, corresponding to a negative gravity anomaly at the south pole. The interpretation of these results is currently under investigation and will reveal crucial information on Enceladus' icy shell structure.

The third Saturnian satellite for which gravity measurements have been performed is Rhea, although the limited dataset (only one pass) makes it difficult to infer robust constraints on the interior of the object. Still, it appears that, like in the case of Enceladus, Rhea's gravity field contains a degree-three component [66, 82]. These authors suggested that the source of that component is the impact basin Tirawa. The mass anomaly associated with the large crater induced a reorientation of the moon's principal axes in order to minimize the rotational energy so that the smallest principal axis moment of inertia is oriented toward the parent-planet, while the largest principal axis moment of inertia presents a small angle from the normal to the orbit, following the Cassini states [87]. More gravity passes of Rhea are required in order to better understand the relationship between its gravity field and topography.

Thomas [108] published the triaxial shapes measured for 20 Saturnian satellites from limb profiles. The global shape of Rhea matches a hydrostatic figure; while for Mimas, Enceladus, and Tethys the degree 2 shapes are not consistent with hydrostatic equilibrium [82, 108]. Consequently, lateral variations in topography or internal structure (e.g. mass concentrations) need to be accounted for in the interpretation of the gravity measurements as these features can bear a non-negligible signature at high-degree spherical harmonics [82].

5.5 Internal Stress

5.5.1 Introduction

In the previous section, we focused on the constant part of the tidal potential that determines a satellite's triaxial shape. We now focus on the time-varying potential induced by eccentricity, obliquity, or physical librations (i.e. oscillations superimposed on the uniform rotation component, e.g. [46, 93]). This source of stress has profound impact on the interior and surface of the satellite. The deformation of the satellite results in friction within the material resulting in the satellite's response being out of phase with respect to the tidal forcing. This friction generates heating. When the tidal heat production exceeds the amount of heat that can be transferred to the satellite's surface, partial melting of the material ensues, and volcanism becomes

the more efficient vector of heat [77]. The most spectacular expression of tidal heating is certainly the active volcanism on Io (Sect. 5.5.3). In the case of icy bodies, cryovolcanism acts at lower temperature, as observed on Enceladus, and suggested for Titan, Triton, Miranda, and Ganymede (Sect. 5.5.4). Also, the stress incurred by the periodic tidal distortion of a satellite's surface can lead to fracturing and drive tectonic activity (Sect. 5.5.5).

5.5.2 Tidal Heating from Mechanical Energy Dissipation

There are two approaches for the computation of tidal heating in satellites. The first one consists in computing the heat produced at each point of the body by using the strain-stress tensor resulting from the tidal distortion. This method has been employed in a series of paper (e.g. [89, 99, 112]) and it enables the quantification of the heat production in each part of the body. However modeling realistic, radially and laterally heterogeneous bodies with this method requires sophisticated numerical codes. In this chapter we focus on another, simpler approach that applies at the global scale of the object, but is equivalent to the former. It is based on the computation of the work performed by the tides (e.g. [118]).

The dissipated energy is equal to the work rate of the tidal force. That work rate is equal to the scalar product of the tidal force $\rho \nabla U$ (where ρ is the material density and U the tidal perturbed potential defined in Sect. 5.2) and the velocity $\mathbf{v}$ of an element of the body integrated over the volume:

$$\frac{dE}{dt} = -\int_{body} \rho \mathbf{v}.\nabla U \, dV. \tag{5.65}$$

The volume integral can be transformed into a surface integral by assuming that the interior is incompressible and homogeneous. Then we obtain

$$\frac{dE}{dt} = -\rho \int_{body} U \, \mathbf{v}.\mathbf{n} \, dS \tag{5.66}$$

by Gauss' theorem. Here $\mathbf{n}$ is the normal to the surface and the quantity $\mathbf{v}.\mathbf{n}$ is the rate at which the surface is elevated. The phase lag between the potential U and the elevation of the surface is then introduced as

$$\zeta = h_2 \frac{U'}{g} \tag{5.67}$$

where h_2 is the dynamic Love number quantifying the deformation of the object (integrated over its radius) and U' is the tidal potential lagged because of friction inside the body. Then, after computing the tidal potential and averaging over the orbital period (short period), tidal dissipation is found as (e.g. [31, 50, 65, 89, 99, 119])

$$\frac{dE}{dt} = -\frac{21}{2} \frac{k_2}{Q} \frac{R_s^5 n^5}{G} e^2. \tag{5.68}$$

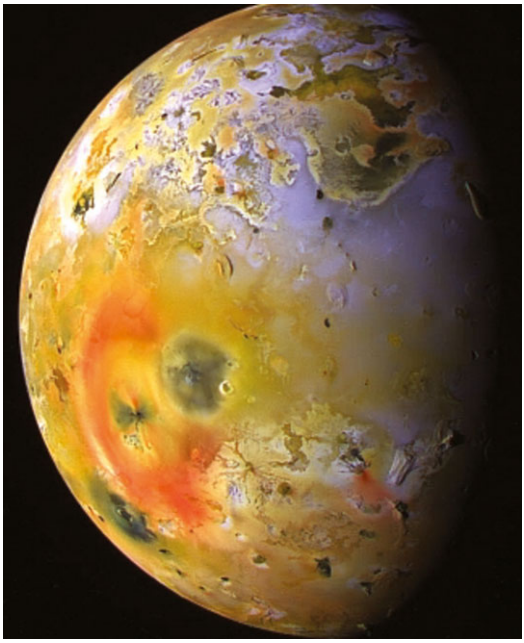

Fig. 5.4 Global view of Jupiter's moon Io taken by Galileo in September 1997. This composite image has color enhanced in order to highlight different regions such as *big red ring* of Pele volcano at the *bottom left*. The *dark spot* close to the *center* of the image was a new distinctive structure illustrating the ongoing activity on Io (http://photojournal.jpl.nasa.gov/catalog/PIA01667), courtesy of NASA

This expression applies to a satellite in synchronous spin-orbit resonance with negligible obliquity, orbital inclination, as well as physical libration. The general expression taking into account these additional perturbations can be found in Wisdom [119] and Levrard [63]. The power of 5 applying to the moon's radius and mean motion implies increased heating in large satellites and/or satellites close to their parent-planets. In addition, the amount of dissipated energy depends on the orbital eccentricity (e^2). This dependency is related to the source of the tidal work being the radial and diurnal tides presented in Sect. 5.3.3.4. The contribution of the librational tides is 4/3 larger than the contribution of the radial tides and the sum of the two contributions leads to the factor 21/2. Finally, the energy rate depends on the ratio k_2/Q that is function of the capacity of the satellite interior to deform and dissipate mechanical energy, which is itself a function of the forcing frequency (Sect. 5.3).

5.5.3 A Hot Satellite: Io

The spacecraft *Voyager 1* revealed in 1979 a unique volcanic world, Io, with active lava flows, volcanic plumes several hundred kilometer high, and a young surface devoid of impact craters [68, 101]. The *Galileo* image displayed in Fig. 5.4, shows Io in false color in order to enhance the different geological structures, where the white and gray features represent sulfur dioxide frost, whereas the bright red and

black features are related to recent volcanic activity. In addition, *Galileo* detected eruptions and identified a recent ring of reddish material deposits around an area called Tvashtar Catena [58, 68].

Io's thermal emission has been inferred from *Galileo*'s data between 1.2 $\mathrm{W\,m^{-2}}$ and 3 $\mathrm{W\,m^{-2}}$ [95, 115] and the global power has been found between 50 and 125 TW. For comparison, Earth's global dissipation budget is around 3.3–4 TW [30], i.e., 25 times smaller. In comparison, other internal heat sources (accretional, radiogenic heating and specific gravitational energy) are several orders of magnitude less significant and insufficient to drive partial melting leading to volcanic activity. This scenario was predicted by Peale et al. [90] a few weeks before the arrival of *Voyager* and developed in more details by, e.g. Moore [77]. The source of energy is related to tides raised by Jupiter on Io that are big due to Io proximity (421 000 km to compare with the Earth-Moon distance of 384 000 km), large Jupiter's mass (300 times the Earth's mass), and a relatively high Io's eccentricity (0.0041). For illustration, the elevation of Io's surface due to the diurnal tides is $3eh_2H$ [16] where e is the eccentricity, h_2 the surface Love number, and H the equilibrium amplitude defined in Eq. (5.1) leading to a surface elevation of about 300 meters height.

It could be surprising that Io kept a non-zero eccentricity because the effect of tides is to circularize the orbit. The eccentricity may be separated in two terms: a free and a forced eccentricity (e.g. [40]). The free eccentricity depends on the initial condition and it is damped to a very small value around 10^{-5} as expected from tidal theory [40]. The forced eccentricity is related to the Laplace resonance Eq. (5.46), and the eccentricity of Io is then pumped by the resonance with Europa and Ganymede that allows the preservation of a non-zero eccentricity until today [40, 88, 121].

This huge amount of energy poses the problem of the transfer of energy from the interior of Io to the surface and the moon's thermal equilibrium. Moore [75] investigated the question of energy transfer by studying convection in a partially molten core and he deduced that the heat that can be transferred is one order lower than the observed flux. This suggests that Io is either out of thermal equilibrium or another heat transport mechanism is taking place. Indeed, the recent determination of Io's dissipation factor determined by Lainey et al. [61] leads to a heat flux equal to $2.24 \pm 0.45\ \mathrm{W\,m^{-2}}$ that is within the range of the observed surface heat flux. In addition, the (k_2/Q) values for Io and Jupiter suggest that Io is close to thermal equilibrium with the energy produced by tidal dissipation being radiated at the surface.

The tidal heating on Io is very unique due to its spectacular consequences that can be seen from Earth (e.g. [115]). However, tidal heating also plays a role on other satellites like Europa where it contributes to the preservation of a deep ocean beneath the icy shell [47, 84, 104, 111]. Ganymede and Miranda may have encountered past resonances that have enhanced their eccentricities and increased their tidal heat budget leading to a possible phase of resurfacing of these satellites (e.g. [23, 100]).

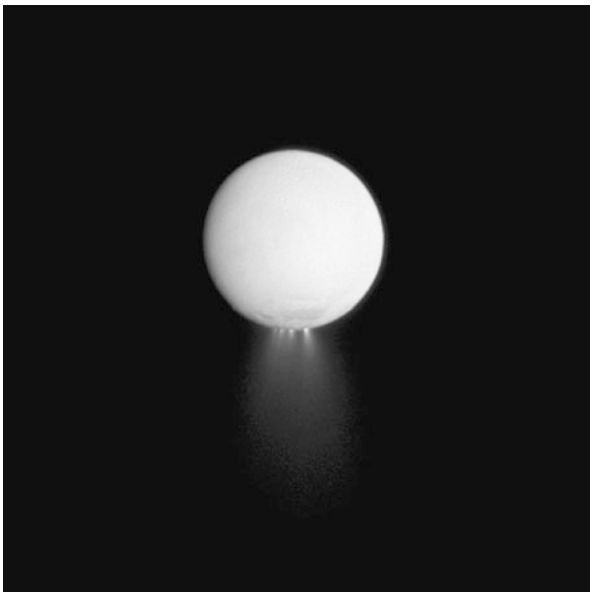

Fig. 5.5 Global view of Enceladus taken by Cassini space mission. The *south pole* presents the famous plumes of water ice burst into the Saturnian system (http://photojournal.jpl.nasa.gov/catalog/PIA12733), courtesy of NASA

5.5.4 Cryovolcanism

Tidal heating can lead to an exotic form of volcanism called *cryovolcanism*, where the volcano erupts liquid or vapor phases of volatile elements such as water ([54] and references therein). The *Voyager*'s observations of Geyser on Neptune's moon Triton [102] or active plumes at the south pole of Enceladus observed by Cassini spacecraft (Fig. 5.5) [91, 106] may suggest that this process, that has no equivalent on Earth, could be widespread in the icy satellites of the outer solar system. However, the existence of cryovolcanism on icy satellites is still debated, as for example in the case of Titan where some cryovolcanic-looking features may actually have a tectonic origin [16, 54, 64, 80, 103]. Nevertheless, signatures of past cryovolcanism have been identified on Europa and Ganymede by the Galileo mission and on Miranda from Voyager imaging (e.g. a review [16]).

Like for Io, Enceladus's cryovolcanism is certainly driven by tidal dissipation [107]. The amount of energy dissipated within Enceladus has been measured by Cassini's Composite Infrared Spectrometer at 5.8 ± 1.9 GW [106] and updated at 15.8 ± 3.1 GW by Howett et al. [45]. Based on the latest measurements of Saturn's dissipation factor, Enceladus is certainly in thermal equilibrium [62]. For Triton, Geyser-like plumes of 8 km height have been observed by *Voyager 2* [102] and the mechanism driving the plumes appears to be recent cryovolcanism that could also explain some enigmatic features and the young age of the Triton's surface [16].

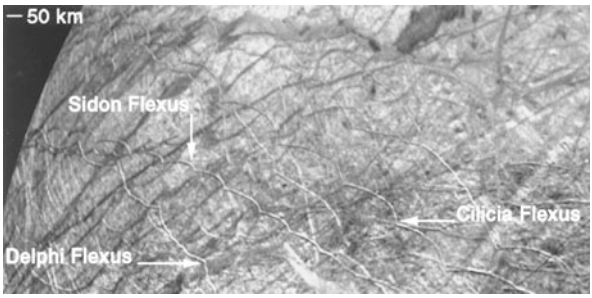

Fig. 5.6 Cycloidal cracks at the surface of Europa (from Hoppa et al. [44])

5.5.5 Tidally Driven Tectonics

Tidal stressing leads to surface fractures at various scales, some of which may run along the entire surfaces of icy satellites. By studying these structures geologists can deduce properties of the surface layer such as its thickness and thermal structure. In addition, the patterns displayed by the geological fractures can reveal key information on the tidal history of the satellites, such as their orbital evolution, reorientation of the outer shell as consequence of decoupling, or non-synchronous rotation of the icy shell (see review in [16], and [56]). Helfenstein and Parmentier [43] first pointed out a correlation between global-scale lineaments patterns and tidal stress in *Voyager* images for Europa. Since then, three types of tectonic features induced by tidal stress have been identified: lineaments, cycloidal cracks, and strike-slip faults (see a review in [8] and references therein). Similar geological structures have recently been identified on Enceladus and Triton, whereas Ganymede and Miranda show past evidence of active tectonics [16].

The icy crust is generally modeled as an elastic layer overlying the tidally deformed body and the tidal stress σ is computed following the formalism developed by Vening-Meinisz [114], Melosh [70]. Compressive stresses are defined when σ is positive and tensional stresses when σ is negative. Fracturation occurs when the tensile stress exceeds the tensile strength of the crust. Then the cracks propagate following the ever-changing stress field and stop where the tensile stress becomes insufficient. Each source of the time-varying potential presents a different stress field whose pattern can be compared against tectonic patterns. Matching the computed field stress with surface cracks can help identify the origin of the tidal stress source and constrain the elastic properties of the crust. For example Fig. 5.6 shows cycloidal cracks on Europa's surface, observed by *Voyager* [101]. These cycloidal structures have been interpreted as the geological consequence of diurnal variations in the tidal stress field [44].

5.6 Conclusion

Tides rhythm the evolution of giant planets satellites like the tides on Earth rhythm the flux and reflux on coasts. Their actions lead to despinning and endogenic activity, such as spectacular volcanism on Io and Enceladus. Tides also bear a signature

in satellites shapes that may be measured if these objects are in hydrostatic equilibrium. However, each satellite also appears to be unique, making the investigation of these systems so fascinating. Many questions are still open and some of them are still under development thanks to the Cassini space mission that has been providing astonishing results. ESA's JUpiter ICy moons Explorer, JUICE, under development [25] will visit the Jupiter system in the next decades (2028) and especially Ganymede and Europa. Even the tidal theory is under an active reevaluation motivated by new laboratory experiments [67] allowing to introduce a more complex rheological response of satellites [13, 27]. In addition, the tidal theory has to introduce the presence of a subsurface ocean, expected in some satellites, that could lead to increased dissipation energy [113].

Acknowledgements Part of this work has been conducted at the Jet Propulsion Laboratory, California Institute of Technology, under contract to the National Aeronautics and Space Administration.

References

1. Aleshkina, E.Y.: Sol. Syst. Res. **43**, 71–78 (2009). doi:10.1134/S0038094609010079
2. Anderson, J.D., Lau, E.L., Sjogren, W.L., Schubert, G., Moore, W.B.: Nature **384**, 541 (1996)
3. Anderson, J.D., Schubert, G., Jacobson, R.A., et al.: Science **281**, 2019 (1998)
4. Anderson, J.D., Jacobson, R.A., Lau, E.L., Moore, W.B., Schubert, G.: J. Geophys. Res. **106**, 32963 (2001)
5. Anderson, J.D., Jacobson, R.A., McElrath, T.P., et al.: Icarus **153**, 157 (2001)
6. Balmino, G.: Artif. Satell. **42**, 141 (2007)
7. Barr, A.C., Citron, R.I., Canup, R.M.: Icarus **209**, 858 (2010)
8. Bills, B.G., Nimmo, F., Karatekin, Ö., Van Hoolst, T., Rambaux, N., Levrard, B., Laskar, J.: Europa. In: Pappalardo, R.T., McKinnon, W.B., Khurana, K.K. (with the assistance of René Dotson with 85 collaborating authors) (eds.) The University of Arizona Space Science Series, vol. 119, p. 119. University of Arizona Press, Tucson (2009). ISBN 9780816528448
9. Carr, M.H., Belton, M.J.S., Chapman, C.R., et al.: Nature **391**, 363 (1998)
10. Cassini, G.D.: Traite de l'Origine et de Progres de l'Astronomie. Paris (1693)
11. Castillo-Rogez, J.C., Lunine, J.I.: Geophys. Res. Lett. **37**, L20205 (2010)
12. Castillo-Rogez, J.C., Matson, D.L., Sotin, C., et al.: Icarus **190**, 179 (2007)
13. Castillo-Rogez, J.C., Efroimsky, M., Lainey, V.: J. Geophys. Res. (Planets) **116**, 9008 (2011)
14. Charnoz, S., Crida, A., Castillo-Rogez, J.C., et al.: Icarus **216**, 535 (2011)
15. Choukroun, M., Sotin, C.: Geophys. Res. Lett. **39**, 4201 (2012)
16. Collins, G., McKinnon, W., Moore, J., Nimmo, F., Pappalardo, R., Prockter, L., Schenk, P.: Tectonics of the outer planet satellites. In: Planetary Tectonics pp. 264–350. Cambridge University Press, Cambridge (2010)
17. Colombo, G.: Astron. J. **71**, 891 (1966)
18. Correia, A.C.M.: Astrophys. J. Lett. **704**, L1 (2009)
19. Darwin, G.H.: Proc. Soc. Lond. Ser. I **30**, 1 (1879)
20. Darwin, G.H.: Philos. Trans. R. Soc. Lond. Ser. I **171**, 713 (1880)
21. Dermott, S.F.: Icarus **37**, 575 (1979)
22. Dermott, S.F., Thomas, P.C.: Icarus **73**, 25 (1988)
23. Dermott, S.F., Malhotra, R., Murray, C.D.: Icarus **76**, 295 (1988)
24. de Sitter, W.: Mon. Not. R. Astron. Soc. **91**, 706 (1931)

25. Dougherty, M., et al.: JUICE: exploring the emergence of habitable worlds around gas giants. ESA/SRE, p. 18 (2011)
26. Ducci, M., Iess, L., Armstrong, J.W., et al.: In: Lunar and Planetary Institute Science Conference Abstracts, vol. 43, p. 2200 (2012)
27. Efroimsky, M.: Celest. Mech. Dyn. Astron. **112**, 283 (2012)
28. Efroimsky, M., Lainey, V.: J. Geophys. Res. **112**, E12003 (2007). doi:10.1029/2007JE002908
29. Efroimsky, M., Williams, J.G.: Celest. Mech. Dyn. Astron. **104**, 257–289 (2009). doi:10.1007/s10569-009-9204-7
30. Egbert, G.D., Ray, R.D.: Nature **405**, 775 (2000)
31. Ferraz-Mello, S., Rodríguez, A., Hussmann, H.: Celest. Mech. Dyn. Astron. **101**, 171 (2008)
32. Fortes, A.D.: Planet. Space Sci. **60**, 10 (2012)
33. Gao, P., Stevenson, D.J.: In: 43rd Lunar and Planetary Institute Science Conference Abstracts, p. 1701 (2012)
34. Gavrilov, S.V., Zharkov, V.N.: Icarus **32**, 443 (1977)
35. Goldreich, P.: Mon. Not. R. Astron. Soc. **126**, 257 (1963)
36. Goldreich, P., Peale, S.: Astron. J. **71**, 425 (1966)
37. Goldreich, P., Soter, S.: Icarus **5**, 375 (1966)
38. Grasset, O., Coustenis, A., Durham, W.B., et al.: Space Sci. Rev. **153**, 5 (2010)
39. Greenberg, R.: Astrophys. J. Lett. **698**, L42 (2009)
40. Greenberg, R.: Rep. Prog. Phys. **73**, 036801 (2010)
41. Greenberg, R., Weidenschilling, S.J.: Icarus **58**, 186 (1984)
42. Greenberg, R., Hoppa, G.V., Bart, G., Hurford, T.: Celest. Mech. Dyn. Astron. **87**, 171 (2003)
43. Helfenstein, P., Parmentier, E.M.: Icarus **53**, 415 (1983)
44. Hoppa, G.V., Tufts, B.R., Greenberg, R., Geissler, P.E.: Science **285**, 1899 (1999)
45. Howett, C.J.A., Spencer, J.R., Pearl, J., Segura, M.: J. Geophys. Res. (Planets) **116**, 3003 (2011)
46. Hurford, T.A., Bills, B.G., Helfenstein, P., et al.: Icarus **203**, 541 (2009)
47. Hussmann, H., Spohn, T., Wiezcerkowski, K.: Icarus **156**, 143–151 (2002)
48. Hussmann, H., Sohl, F., Spohn, T.: Icarus **185**, 258 (2006)
49. Hussmann, H., Sotin, C., Lunine, J.I.: In: Schubert, G., Spohn, T. (eds.) Treatise on Geophysics—Planets and Moons, pp. 509–539. Elsevier, Amsterdam (2007)
50. Hussmann, H., Choblet, G., Lainey, V., et al.: Space Sci. Rev. **153**, 317 (2010)
51. Hut, P.: Astron. Astrophys. **99**, 126 (1981)
52. Ioannou, P.J., Lindzen, R.S.: Astrophys. J. **406**, 266–278 (1993)
53. Iess, L., Rappaport, N.J., Jacobson, R.A., et al.: Science **327**, 1367 (2010)
54. Jaumann, R., Clark, R.N., Nimmo, F., et al.: Saturn from Cassini-Huygens, p. 637 (2009)
55. Jeffreys, H.: Mon. Not. R. Astron. Soc. **122**, 339 (1961)
56. Kattenhorn, S.A., Hurford, T.: Europa. In: Pappalardo, R.T., McKinnon, W.B., Khurana, K.K. (with the assistance of René Dotson with 85 collaborating authors) (eds.) The University of Arizona Space Science Series, vol. 199, p. 199. University of Arizona Press, Tucson (2009). ISBN 9780816528448
57. Kaula, W.M.: Rev. Geophys. Space Phys. **2**, 661 (1964)
58. Keszthelyi, L., et al.: J. Geophys. Res. (Planets) **106**(E12), 33025–33052 (2001)
59. Khurana, K.K., Kivelson, M.G., Stevenson, D.J., et al.: Nature **395**, 777 (1998)
60. Krupp, N., Khurana, K.K., Iess, L., et al.: Space Sci. Rev. **153**(1–4), 11–59 (2010)
61. Lainey, V., Arlot, J.-E., Karatekin, Ö., Van Hoolst, T.: Nature **459**, 957 (2009)
62. Lainey, V., Karatekin, Ö., Desmars, J., et al.: Astrophys. J. **752**, 14 (2012)
63. Levrard, B.: Icarus **193**, 641 (2008)
64. Lopes, R.M.C., Mitchell, K.L., Stofan, E.R., et al.: Icarus **186**, 395 (2007)
65. MacDonald, G.J.F.: Rev. Geophys. Space Phys. **2**, 467 (1964)
66. Mackenzie, R.A., Iess, L., Tortora, P., Rappaport, N.J.: Geophys. Res. Lett. **35**, 5204 (2008)

67. McCarthy, C.M., Castillo-Rogez, J.C.: Planetary ices attenuation properties. In: Gudipati, M.S., Castillo-Rogez, J.C. (eds.) Science of Solar System Ices, pp. 183–226. Springer, New York (2011)
68. McEwen, A.S.: Active volcanism on Io. Science **297**, 2220–2221 (2002)
69. McKinnon, W.B.: Icarus **183**, 435 (2006)
70. Melosh, H.J.: Icarus **43**, 334 (1980)
71. Meyer, J., Wisdom, J.: Icarus **188**, 535 (2007)
72. Mignard, F.: Moon Planets **20**, 301 (1979)
73. Mignard, F.: Moon Planets **23**, 185 (1980)
74. Mignard, F.: Moon Planets **24**, 189 (1981)
75. Moore, W.B.: J. Geophys. Res. **108**, E8 (2003). doi:10.1029/2002JE001943
76. Moore, W.B., Schubert, G.: Icarus **166**, 223 (2003)
77. Moore, W.B., Schubert, G., Anderson, J.D., Spencer, J.R.: In: Io After Galileo: A New View of Jupiter's Volcanic Moon, p. 89 (2007)
78. Munk, W.H., MacDonald, G.J.F.: Cambridge [Eng.] University Press, Cambridge (1960)
79. Murray, C.D., Dermott, S.F.: In: Murray, C.D., Dermott, S.F. (eds.) Solar System Dynamics. Cambridge University Press, Cambridge (2000). ISBN 0521575974
80. Nelson, R.M., Kamp, L.W., Lopes, R.M.C., et al.: Geophys. Res. Lett. **36**, 4202 (2009)
81. Nimmo, F., Bills, B.G.: Icarus **208**, 896 (2010)
82. Nimmo, F., Bills, B.G., Thomas, P.C., Asmar, S.W.: J. Geophys. Res. (Planets) **115**, 10008 (2010)
83. Ogilvie, G.I., Lin, D.N.C.: Astrophys. J. **610**, 477 (2004)
84. Ojakangas, G.W., Stevenson, D.J.: Thermal state of an ice shell on Europa. Icarus **81**, 220–241 (1989)
85. Palguta, J., Schubert, G., Zhang, K., Anderson, J.D.: Icarus **201**, 615 (2009)
86. Pappalardo, R.T., Head, J.W., Greeley, R., et al.: Nature **391**, 365 (1998)
87. Peale, S.J.: Annu. Rev. Astron. Astrophys. **37**, 533 (1999)
88. Peale, S.J.: Celest. Mech. Dyn. Astron. **87**, 129 (2003)
89. Peale, S.J., Cassen, P.M.: Icarus **36**, 245–269 (1978)
90. Peale, S.J., Cassen, P., Reynolds, R.T.: Science **203**, 892–894 (1979)
91. Porco, C.C., Helfenstein, P., Thomas, P.C., et al.: Science **311**, 1393 (2006)
92. Rambaux, N., Castillo-Rogez, J.C., Williams, J.G., Karatekin, Ö.: Geophys. Res. Lett. **37**, 4202 (2010)
93. Rambaux, N., Van Hoolst, T., Karatekin, Ö.: Astron. Astrophys. **527**, A118 (2011)
94. Rappaport, N.J., Iess, L., Wahr, J., et al.: Icarus **194**, 711 (2008)
95. Rathbun, J.A., Spencer, J.R., Tamppari, L.K., Martin, T.Z., Barnard, L., Travis, L.D.: Icarus **169**, 127–139 (2004). 12.021. doi:10.1016/j.icarus.2003
96. Schaefer, B.E., Tourtellotte, S.W., Rabinowitz, D.L., Schaefer, M.W.: Icarus **196**, 225 (2008)
97. Schubert, G.: Nature **459**, 920 (2009)
98. Schubert, G., Anderson, J.D., Spohn, T., McKinnon, W.B.: Jupiter: The Planet, Satellites and Magnetosphere, p. 281 (2004)
99. Segatz, M., Spohn, T., Ross, M.N., Schubert, G.: Icarus **75**, 187–206 (1988)
100. Showman, A.P., Malhotra, R.: Icarus **127**, 93 (1997)
101. Smith, B.A., Soderblom, L.A., Beebe, R., et al.: Science **206**, 927 (1979)
102. Soderblom, L.A., Becker, T.L., Kieffer, S.W., Brown, R.H., Hansen, C.J., Johnson, T.V.: Science **250**, 410–415 (1990)
103. Sotin, C., Jaumann, R., Buratti, B.J., et al.: Nature **435**, 786–789 (2005)
104. Sotin, C., Tobie, G., Wahr, J., McKinnon, W.B.: Europa, In: Pappalardo, R.T., McKinnon, W.B., Khurana, K.K. (with the Assistance of René Dotson with 85 collaborating authors) (eds.) The University of Arizona Space Science Series, vol. 85, p. 85. University of Arizona Press, Tucson (2009). ISBN 9780816528448
105. Sotin, C., Mitri, G., Rappaport, N., Schubert, G., Stevenson, D.: Titan from Cassini-Huygens, p. 61 (2010)
106. Spencer, J.R., Pearl, J.C., Segura, M., et al.: Science **311**, 1401 (2006)

107. Spencer, J.R., Barr, A.C., Esposito, L.W., et al.: Saturn from Cassini-Huygens, p. 683 (2009)
108. Thomas, P.C.: Icarus **208**, 395 (2010)
109. Thomas, P.C., Davies, M.E., Colvin, T.R., et al.: Icarus **135**, 175 (1998)
110. Thomas, P.C., Burns, J.A., Helfenstein, P., et al.: Icarus **190**, 573 (2007)
111. Tobie, G., Choblet, G., Sotin, C.: J. Geophys. Res. **108** (2003). doi:10.1029/2003JE002099
112. Tobie, G., Mocquet, A., Sotin, C.: Icarus **177**, 534–549 (2005)
113. Tyler, R.H.: Nature **456**, 770 (2008)
114. Vening-Meinisz, F.A.: Trans. AGU **28**, 1–61 (1947)
115. Veeder, G.J., Davies, A.G., Matson, D.L., et al.: Icarus **219**, 701 (2012)
116. Wahr, J.M., Zuber, M.T., Smith, D.E., Lunine, J.I.: J. Geophys. Res. (Planets) **111**, 12005 (2006)
117. Ward, W.R.: Icarus **46**, 97 (1981)
118. Wisdom, J.: Astron. J. **128**, 484–491 (2004)
119. Wisdom, J.: Icarus **193**, 637 (2008)
120. Wisdom, J., Peale, S.J., Mignard, F.: Icarus **58**, 137 (1984)
121. Yoder, C.F.: Nature **279**, 767 (1979)
122. Yoder, C.F.: In: Global Earth Physics. A Handbook of Physical Constants (1995)
123. Yoder, C.F., Peale, S.J.: Icarus **47**, 1 (1981)
124. Zebker, H.A., Stiles, B., Hensley, S., et al.: Science **324**, 921 (2009)
125. Zharkov, V.N., Leontjev, V.V., Kozenko, V.A.: Icarus **61**, 92 (1985)